

Temporal precipitation variability versus altitude on a tropical high mountain: Observations and mesoscale atmospheric modelling

Thomas Mölg,^{ab*} John C.H. Chiang,^a Alexander Gohm^c and Nicolas J. Cullen^d

^aCenter for Atmospheric Sciences and Department of Geography, University of California at Berkeley, USA

^bCenter for Climate and Cryosphere, Department of Geography, University of Innsbruck, Austria

^cCenter for Climate and Cryosphere, Institute of Meteorology and Geophysics, University of Innsbruck, Austria

^dDepartment of Geography, University of Otago, New Zealand

ABSTRACT: The occurrence of maximum precipitation amounts (P_{\max}) on tropical high mountains at mid elevations is well documented (spatial variability), but little is known about the temporal variability of precipitation in different elevation zones. The present study targets this issue by combining various types of observations on and around Kilimanjaro (East Africa, 5895 m a.s.l.) with mesoscale atmospheric modelling. In observations, the vertical moisture profiles of air masses approaching the mountain clearly differ during ‘normal’ and ‘significant’ daily precipitation events on Kilimanjaro’s summit, while model experiments illustrate that the elevation zone of P_{\max} is shifted upslope substantially during the latter events. Large (small) differences in precipitation therefore appear in the dry (moist) high-elevation (mid- and low-elevation) zones of the mountain. This space–time pattern is evident in observations of seasonal precipitation variability on Kilimanjaro and on nearby Mount Kenya for anomalous wet seasons, which are controlled by the frequency of ‘significant’ daily events. The upslope shift of P_{\max} in the model is favoured by dynamical factors (stronger air ascent and higher static instability of clouds), microphysical processes (greater efficiency in converting condensate to precipitation over high-elevation terrain), and related feedback mechanisms (stronger latent heating). Beyond the seasonal scale, tropical climate change also entails changed frequencies of dry- and moist-air advection, which is demonstrated for the Kilimanjaro region over 1979–2006. Thus, long-term changes of precipitation are probably most drastic in the dry summit zones of tropical high mountains. Copyright © 2009 Royal Meteorological Society

KEY WORDS Tropics; orographic precipitation; Kilimanjaro; mesoscale circulation

Received 5 May 2008; Revised 15 April 2009; Accepted 11 May 2009

1. Introduction

Mountains are known to significantly modify large-scale atmospheric flow and therefore create a local- and regional-scale climate that may differ drastically from the adjacent plains. This is most apparent in the precipitation climatology, a prominent example of which is the Atacama Desert in the ‘rain shadow’ of the Andes – illustrating that mountains can be climatic divides in the most extreme case (e.g. Roe, 2005). Hence, research on orographic precipitation has always provided a particular stimulus to the atmospheric sciences. Recent overviews of such research are given by Roe (2005) and Rotunno and Houze (2007). In general, orographic precipitation is classified into two types: stratiform orographic precipitation that follows from stable and forced ascent of moist air, and convective precipitation which involves unstable ascent (and the presence of buoyant instability) triggered or enhanced by the mountain. However, the transition between the two may be blurred in the real world, for

instance when shallow convection is embedded in stratiform orographic clouds (Kirshbaum and Durran, 2004; Fuhrer and Schär, 2005).

Capturing the spatial distribution of precipitation on mountains is difficult, but regional studies have shown from observations (e.g. Hemp, 2006) or a combination of observations and mesoscale atmospheric modelling (e.g. Bormann and Marks, 1999; Rögnvaldsson *et al.*, 2007) that mountains enhance precipitation, and amounts tend to increase at higher elevations compared to the lowlands. This effect is most pronounced in situations when slopes face dominant wind directions (Dettinger *et al.*, 2004). While precipitation on mountains in the extratropics (especially at high latitudes) generally increases upslope with maxima in the vicinity of the summit areas (e.g. Rögnvaldsson *et al.*, 2007), rainfall on tropical high mountains maximizes at mid elevations (Hastenrath, 1991). The decrease towards the peak results from the mostly convective nature of tropical precipitation, where the moisture content in the atmospheric column, as well as the precipitable water in the convective cloud, drop above the characteristic ‘belt’ of maximum precipitation (Hastenrath, 1991).

*Correspondence to: Thomas Mölg, Department of Geography, University of Innsbruck, Innrain 52, A-6020 Innsbruck, Austria. E-mail: thomas.moelg@uibk.ac.at

The interaction between mountains and the large-scale flow not only results in complex precipitation patterns in mountainous terrain, but also generates distinct circulation types. Schär (2002) reviewed this topic, including flow stagnation and retardation, gravity wave breaking, and flow separation. He emphasizes that such processes can occur over large spatial scales and even impact planetary-scale waves. The present study targets the mesoscale, and focuses on the relationship between precipitation patterns and modification of the atmospheric flow over a tropical high mountain: Kilimanjaro (5895 m above sea level (a.s.l.)). Africa's highest massif, and one of the largest free-standing mountains in the world, is located in equatorial East Africa at the Tanzania–Kenya border (3.1°S/37.4°E). The next section describes the background of this choice and the specific goals of the paper.

2. Background and goals

The characteristic vertical pattern of precipitation on tropical mountains is also present on Kilimanjaro. Røhr and Killingtveit (2003) and Hemp (2006) show from meteorological measurements on the southern slope of the mountain that the zone of maximum precipitation (~ 2500 mm year⁻¹) is located at ~ 2200 m a.s.l., and coincides with the zone of montane forest. The temporal distribution of precipitation in the Kilimanjaro region follows a bimodal pattern with wet seasons from March to May (MAM) and October to December (OND), separated by a pronounced dry season (JJAS, June–September) (e.g. Indeje *et al.*, 2000). A moderate dry season occurs in January and February (JF). Hygric seasonality also dominates the climate in the glaciated summit region of Kilimanjaro on the central peak Kibo (Figure 1), as revealed by high-altitude measurements (Hardy, 2003; Mölg *et al.*, 2008a, 2009a, 2009b).

Precipitation in East Africa, including the Kilimanjaro region, depends critically on moisture supply from the Indian Ocean. Its importance has been extensively investigated in connection with intraseasonal and interannual precipitation variability (e.g. Webster *et al.*, 1999; Mutai and Ward, 2000), interdecadal fluctuations (e.g. Clark *et al.*, 2003), and is also evident in long-term changes of East African precipitation (e.g. Hastenrath, 2001; Mölg *et al.*, 2006). A recent study by Chan *et al.* (2008) highlighted this linkage on the synoptic scale: by comparing selected MAM and OND snowfall events recorded at automatic weather station (AWS) 1 on Kibo's summit (Figure 1) with the large-scale circulation as captured by reanalysis data, they confirm the Indian Ocean as the primary source of moisture. Only during MAM does moisture from the interior of the African continent appear to contribute to snowfall on Kilimanjaro.

Understanding the processes responsible for changes to glaciers on Kibo has led to the recent interest in precipitation on Kilimanjaro (Mölg and Hardy, 2004; Cullen *et al.*, 2006; Mölg *et al.*, 2008a). Glaciers on Kibo receded significantly between the 1880s and 2003

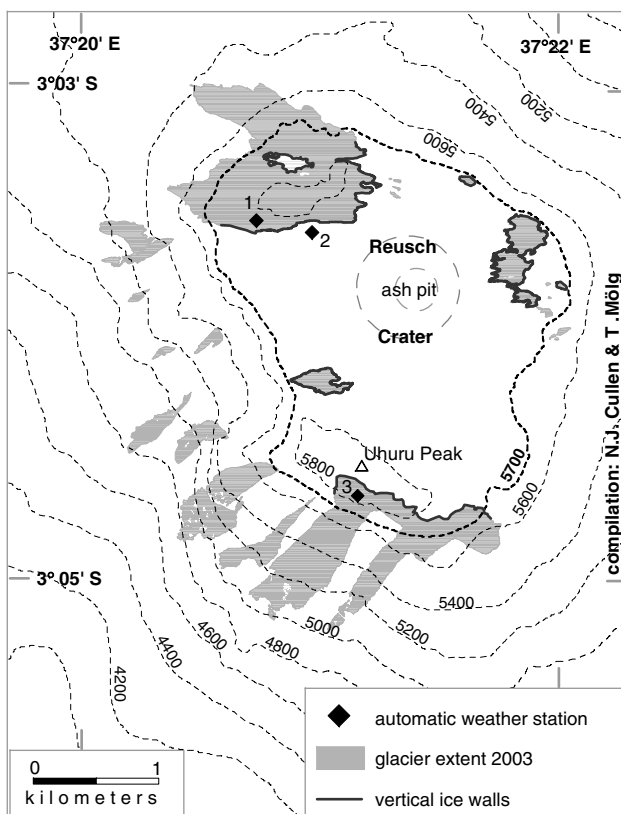


Figure 1. Glaciers on Kibo in 2003 (Cullen *et al.*, 2006) and the locations of automatic weather stations, vertical ice cliffs/walls, the eruption cone (Reusch Crater), and Africa's highest point (Uhuru Peak, 5895 m). The highlighted 5700 m contour roughly delineates the summit plateau. Map projection is Universal Transverse Mercator (UTM), zone 37S, with contours in metres above sea level (interval is 200 m).

(Cullen *et al.*, 2006), and the cause has been definitively linked to decreases in precipitation by studying the glaciers' mass and energy budgets (Mölg and Hardy, 2004; Mölg *et al.*, 2008a, 2009b). Drought conditions in the 20th century have also been inferred in the surrounding regions from vegetation changes (Hemp, 2005), problems in the productivity of Maasai pastoralists (Mwangi and Desanker, 2007), historical-source proxy data (Hastenrath, 2001), low lake levels (Nicholson and Yin, 2001), and palaeoclimate simulations with coupled atmosphere–ocean general circulation models (Mölg *et al.*, 2006).

In summary, the studies above have improved our understanding of local precipitation patterns on Kilimanjaro as well as of the large-scale circulation that controls weather and climate in East Africa and the Kilimanjaro region. However, the link between these two scales represents a gap of knowledge: the mesoscale interaction of the huge mountain with the air masses of the large-scale flow. This interaction is not resolved in the gridded datasets used to analyse large-scale circulation (Chan *et al.*, 2008), but is assumed to have a major impact on precipitation (section 1) and is thus critical for the analysis of the observed glacier shrinkage on Kibo. The present study targets this gap in the context of the mesoscale circulation, and its relationship with the temporal precipitation

variability in different elevation zones on Kilimanjaro. Specific goals are therefore:

- (1) to examine the seasonal variability of measured precipitation for the summit of Kilimanjaro and the surrounding lowlands;
- (2) to analyse the atmospheric conditions (in particular temperature, moisture and stability) of the air masses approaching Kilimanjaro (the ‘background flow’), and how they relate to the transition from dry to wet events on Kilimanjaro’s summit; and
- (3) to simulate the vertical profile of precipitation on the mountain in relation to the background flow with an atmospheric model, to better understand the vertical characteristics of the observed seasonal precipitation variability.

3. Methods, data and modelling

Our methodology is based on direct field measurements at high altitude (section 3.1) that help to define three different moisture classes of daily meteorological conditions on Kibo’s summit. This classification (section 3.2) does not aim to categorize all available days, but to create a best possible contrast between the three classes. Given this framework and the specific goals, the methodology is structured as follows:

- First, both the sign and magnitude (amplitude) of the seasonal precipitation variability observed in different elevation zones are analysed statistically.
- Second, the atmospheric variability of the background flow in National Centers for Environmental Prediction/National Center for Atmospheric Research (NCEP/NCAR) reanalysis data (Kalnay *et al.*, 1996) is examined for the three moisture classes through empirical orthogonal functions (EOFs, e.g. Mutai and Ward, 2000; Mölg *et al.*, 2006).
- Third, selected vertical profiles of the background flow from each class are used as input to a numerical atmospheric model (section 3.3), which simulates circulation and precipitation patterns on Kilimanjaro.

3.1. Observations

High-altitude measurements are conducted at three AWSs in the summit zone of Kibo (Figure 1; station 1 operated by the University of Massachusetts, 2 and 3 by Innsbruck). AWS3 is almost directly located at Africa’s highest point on a key glacier for revealing climate change at this high altitude (Mölg *et al.*, 2008a), and is therefore used as the data source for this study. Gap-free records for nearly two years are available between 9 February 2005 and 9 January 2007 for global radiation and reflected short-wave radiation, incoming and emitted long-wave radiation, air temperature and humidity at two levels, wind speed and direction, air pressure, and surface height

change (half-hourly means for all). For details of instruments, data treatment and storage, and weather conditions at AWS3 refer to e.g. Mölg *et al.* (2008a, 2009a). In brief, mean air temperature at AWS3 (5873 m a.s.l., 502 hPa) is -7°C and daily mean values fluctuate $<4^{\circ}\text{C}$ around this value. Moderate mean wind speeds (5 m s^{-1}) and high mean global radiation (333 W m^{-2}) further characterize the weather at this site. Daily precipitation (mostly snow accumulation) is shown in Figure 2, constructed from the surface height change data (e.g. Mölg and Hardy, 2004). The record exhibits the MAM and OND wet seasons, apart from OND 2005 which was anomalously dry (Hastenrath *et al.*, 2007). OND 2006, in contrast, brought abundant snowfall and anomalously strong precipitation over East Africa (discussed further in section 4.3), probably due to the ENSO event in 2006/2007. El Niño initiates a Tropics-wide teleconnected response (Chiang and Lintner, 2005), and does show a signature in East African wet seasons (above-average precipitation) on the climatological record (Indeje *et al.*, 2000). The average annual precipitation estimate from the AWS3 record (Figure 2) is 391 mm (water equivalent) by using a minimum fresh snow density $\rho_{\text{fs}} = 200\text{ kg m}^{-3}$ (Mölg *et al.*, 2008a). This value of $\sim 400\text{ mm}$ illustrates well the decrease in precipitation between the low-elevation zone of maximum precipitation ($\sim 2500\text{ mm year}^{-1}$) and the summit.

Data from the Tropical Rainfall Measuring Mission (TRMM, e.g. Huffman *et al.*, 2007) are used to obtain area-integrated precipitation at a resolution high enough to represent the surrounding lowlands of Kilimanjaro. The chosen TRMM product is 3B43, which merges satellite data with rain gauge data at a horizontal resolution of 0.25° and on a monthly scale. This international joint project maintains a dedicated website, including links to data description and access (<http://trmm.gsfc.nasa.gov/>).

We utilize NCEP/NCAR reanalysis (REA) data (Kalnay *et al.*, 1996) to analyse the air masses approaching Kilimanjaro. Data are extracted for the grid point at 2.5°S and 37.5°E , east of Kilimanjaro. The frequency

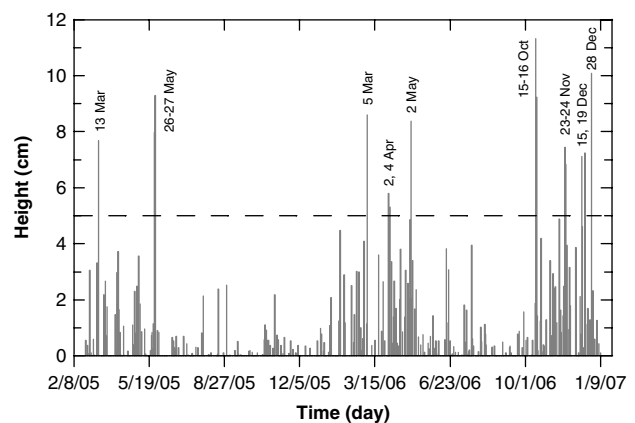


Figure 2. Daily snow accumulation at AWS3 on Kibo (5873 m a.s.l.) between 9 February 2005 and 9 January 2007 (days: m/d/yy). The dashed line shows the threshold of 5 cm used to select ‘significant’ snowfall events on Kibo’s summit (see text, section 3.2).

distribution of wind directions recorded on Kibo's summit shows a dominant maximum (72%) of easterly winds (45° – 135°) at AWS3, and so do the REA data at 500 hPa (66%). REA reveals that easterly winds also dominate at lower levels, and the peak in the frequency distribution of all winds between the surface and 500 hPa lies in the sector 45° – 90° from north. Furthermore, the four grid points surrounding Kilimanjaro show a mean altitude of only 1231 m a.s.l., indicating that the REA assimilation process is not disturbed by a high mountain. Taken together, it suggests that the chosen grid point is representative of the large-scale flow upstream of Kilimanjaro.

REA can be a pure model product in the observation-sparse Tropics, but is closely related to nearby observations if these are representative of the REA grid box and are therefore assimilated into the system (e.g. Schafer *et al.*, 2003). The rawinsonde launches at Nairobi (WMO station 63 741) deliver observations close to our chosen grid point and do enter the assimilation process. Data are thus constrained by observations, which are detailed in the results (section 4.3).

3.2. Classification of moisture and precipitation events on Kilimanjaro

The three moisture classes defined here refer to meteorological conditions in the summit area of Kibo. Precipitation amount is the central criterion. Daily snowfall >5 cm (actual height) is classified as a 'significant' snowfall event (SIG class; $N = 14$ days, mean snowfall is 8 cm day^{-1}). This threshold captures the very largest snowfall events in the record (Figure 2). The 'normal' snowfall class (NORM class; $N = 41$ days) covers daily snowfall amounts of 1–2 cm; this is where the peak in the frequency distribution occurs. Since measured surface height changes <1 cm approach the maximum accuracy of the employed instrument (e.g. Mölg and Hardy, 2004), 'normal' may also be understood as events with minimum snowfall amounts. Convection and precipitation in the Tropics mainly occur in the afternoon (Hastenrath, 1991), and strong events on Kibo's summit are rather brief in duration and sometimes dominated by graupel (Hardy, personal communication; Winkler, personal communication). Assuming that precipitation falls within 3–4 hours in the afternoon and has a density of roughly 250 ± 50 kg m^{-3} (Mölg *et al.*, 2009b) the precipitation rate (P_r) during SIG and NORM events is in the order of 3–6 and 0.5–1.5 mm h^{-1} , respectively.

Finally, we define a class of 'very dry' conditions on Kibo's summit (DRY class; $N = 59$ days). The days assigned to this class were selected by Mölg *et al.* (2009a) as 'clear-sky days' for the summit area (i.e. no clouds and precipitation) on the basis of high solar radiation, low net long-wave radiation, and low relative humidity at AWS3.

To examine whether the three classes indeed reflect moisture conditions as a whole, Table I lists other relevant variables for each class. This test confirms that the order SIG, NORM and DRY does display the transition from very wet to very dry conditions. Furthermore, the classes

incorporate a strong seasonal signal. All SIG events occurred in the wet seasons (Figure 2), and the majority of NORM events also did (30 of 41). Forty-seven of 59 DRY events occurred in the climatological dry seasons (and 12 more in the anomalously dry OND 2005).

3.3. The numerical atmospheric model and experimental design

The Regional Atmospheric Modeling System (RAMS), developed at Colorado State University (Pielke *et al.*, 1992; Cotton *et al.*, 2003), is based on fully compressible and non-hydrostatic primitive equations. They are solved for an Arakawa C-grid in the horizontal on a polar stereographic projection, while in the vertical a terrain-following coordinate is used (Gal–Chen scaled-height). The time dimension relies on a hybrid form of leapfrog and forward-in-time differencing. RAMS comes with a package of sophisticated physical parametrizations (Cotton *et al.*, 2003), which are detailed further below. Model forcing at the lateral boundaries can be variable (by nesting in a global REA or climate model) or horizontally homogeneous (by a single sounding that specifies the background flow).

In this study we conduct idealized simulations that employ bell-shaped topography and horizontally homogeneous forcing (see Rotunno and Houze, 2007), using soundings for temperature, moisture and the wind (which are determined in section 4). An isolated bell-shaped mountain is defined by a Witch of Agnesi function with a horizontal half-width (a) of 10 km, a height of 5895 m, and a horizontal resolution $\Delta x = \Delta y = 1$ km. The domain size comprises $20a$ (200 grid points) in each horizontal direction (e.g. Jiang, 2003). Figure 3(a) shows the model's Kilimanjaro region, and illustrates that the simple bell shape follows quite closely a more realistic topography obtained from the Shuttle Radar Topography Mission (Rabus *et al.*, 2003). The half-width of 10 km is chosen to reasonably match the real horizontal dimension at higher elevations (>4000 m a.s.l.), since cloud development in these regions often determines whether or not the summit zone experiences moist conditions (Kaser and Osmaston, 2002). The 48 levels in the vertical reach to a height of ~ 19.7 km (ordinate in Figure 3(b)). The finest resolution ($\Delta z = 80$ m) at the surface increases by a stretch factor of 1.15 to a maximum spacing of 500 m (at ~ 3.7 km height) above which it is held constant (e.g. Gohm and Mayr, 2005). The time step Δt for the integrations is 4 seconds (and 2 seconds for the terms concerning the propagation of sound).

Regarding the physical parametrizations, turbulence closure is calculated from a deformation-based Smagorinsky scheme with stability modification (see Cotton *et al.*, 2003), both for horizontal and vertical diffusion coefficients. Horizontal mixing is computed along truly horizontal instead of terrain-following coordinates, to avoid numerical noise due to steep topography (Zängl *et al.*,

Table I. Snowfall criteria used to define classes of significant snowfall (SIG), normal snowfall (NORM), and very dry conditions (DRY) at AWS3 in the period 9 February 2005 to 9 January 2007.

Criterion or Variable	SIG class ($N = 14$ days)	NORM class ($N = 41$ days)	DRY class ($N = 59$ days)
Daily snowfall amount (cm)	>5	1–2	0
Global radiation (W m^{-2})	233	296	380
Incoming long-wave radiation (W m^{-2})	280	223	128
Relative humidity (%)	87	73	19
Daily maximum water vapour pressure (hPa)	5.1	4.1	1.9
Horizontal wind speed (m s^{-1})	2.3	4.1	5.3
Potential instability strength (K)	23.0 (10.2)	23.8 (10.7)	15.0 (4.7)

Variables other than snowfall are averaged over all days in the respective class. The last row shows the strength of the potential instability in the background flow based on NCEP/NCAR reanalysis data (to be discussed in section 4.2), with 1σ in brackets.

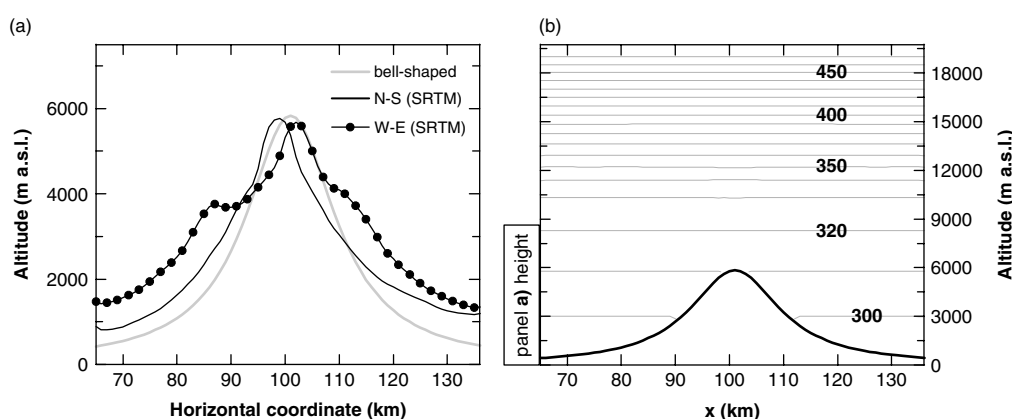


Figure 3. Vertical cross-sections through the domain centre of (a) the model relief (bell-shaped and as a comparison from the Shuttle Radar Topography Mission (SRTM) data for north–south and west–east sections), and (b) potential temperature in the ‘numerical stability experiment’ after 12 hours of integration (10 K spacing). Note the different vertical exaggerations of the plots.

2004). An initial dry experiment serves to check numerical stability in this context, where we use a standard-atmosphere temperature stratification, zero-wind conditions and no moisture (see Zängl *et al.*, 2004). Figure 3(b) reveals that – after 12 hours of integration – the field of potential temperature is virtually undisturbed; thus, we do not expect numerical errors from the horizontal mixing scheme. Given the high spatial horizontal resolution, convection is not parametrized but assumed to be resolved explicitly (e.g. Gohm and Mayr, 2005). The cloud microphysics scheme in RAMS (Walko *et al.*, 1995) includes liquid and solid precipitation, and groups hydrometeors into seven categories (cloud water, rain, snow, pristine ice, aggregates, graupel, hail). The concentrations of these hydrometeors are prognostically determined by the model, based on a fixed number of cloud condensation nuclei ($3 \times 10^8 \text{ kg}^{-1}$ or $\sim 400 \text{ cm}^{-3}$).

For the lower boundary, a ‘no-slip’ condition is prescribed by a roughness length of 0.5 m, so vertical fluxes of momentum are allowed. Surface heating is simulated by prescribing a temperature difference between the surface and the lowest atmospheric grid points ($T_{\text{dsa}} = 1 \text{ K}$). The value of T_{dsa} was found by tuning to reproduce the observed precipitation rate in the summit zone (section 3.2). The resultant domain-average heat flux into

the atmosphere using this temperature difference, around 40 W m^{-2} , is in close agreement with the net heat flux derived from the REA model. The sensitivity of the results to T_{dsa} is discussed in section 4.3. Lateral boundary conditions rely on the Klemp–Wilhelmson formulation for the normal velocity components (Klemp and Wilhelmson, 1978), and a zero-gradient condition for all other variables. At the upper boundary, a Rayleigh damping layer between $\sim 14.2 \text{ km}$ and the model top prevents possible downward reflection of gravity waves and other disturbances.

All simulations are integrated to $t = 5$ hours. Horizontally homogeneous simulations are typically in a quasi-steady state after ~ 3 hours, which means averaged fields stay nearly constant (Fuhrer and Schär, 2005). We also find this for our experiments (sections 4.3 and 4.4) and evaluate the results from the output between $t = 3$ and five hours (e.g. Fuhrer and Schär, 2005).

4. Results and discussion

4.1. Observed precipitation at high and low altitude

In the remainder of the paper, the time-variability of precipitation is mostly viewed as a relative deviation from

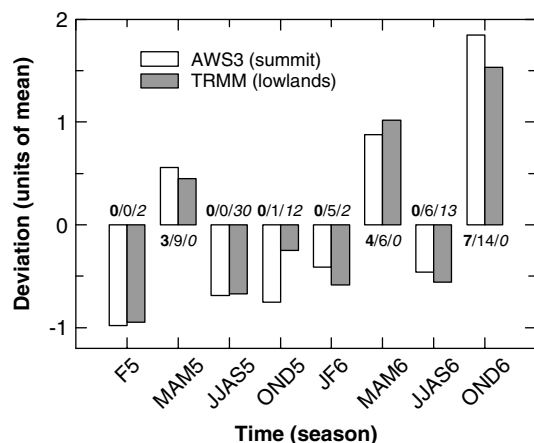


Figure 4. Seasonal precipitation variability (deviation in units of monthly mean per month) at AWS3 and the surrounding lowland of Kilimanjaro (TRMM data, averaged over all directions) between February 2005 and December 2006. The number of days from the three defined moisture classes (section 3.2) are displayed for each season in bold (significant snowfall), normal (normal snowfall), and italics (very dry conditions).

a reference (mean) value, because precipitation totals vary so strongly with elevation on tropical mountains (as detailed in sections 1 and 2). Figure 4 shows the precipitation variability at 5873 m a.s.l. (AWS3) and the surrounding lowlands of Kilimanjaro. For the latter the four grid cells from the TRMM data to the north, east, south and west of the Kilimanjaro grid cell are extracted. The mean annual precipitation of these four cells varies between 774 and 1022 mm. This is the typical amount for lowlands at the base of the mountain, for instance as measured in Moshi to the south of Kilimanjaro (956 mm at 813 m a.s.l., see Fig. 12.1 in Mölg *et al.*, 2008b). There is a clear consistency of seasonal precipitation variability, which shows the same sign at low and high altitudes (Figure 4). The magnitude of the deviations in the dry seasons is very similar, while it tends to differ in some of the climatological wet seasons. This applies to the anomalously dry OND 2005 and to the anomalously wet OND 2006. Hence, the relative range of seasonal precipitation variability is greater in the dry high-elevation zone than in the moister lowlands. A similar pattern of moisture variability versus altitude was detected for other tropical mountains on annual and smaller time-scales from specific humidity (Garreaud *et al.*, 2003) and atmospheric long-wave radiation (Mölg *et al.*, 2009a).

4.2. Observed variability of the background flow in different moisture classes

Here we analyse the 1200 UTC (1500 local time) REA data at the grid point east of Kilimanjaro (section 3.1), as they coincide with the time of day when precipitation on Kibo usually falls (see section 3.2). Furthermore, the variability of the equivalent potential temperature (θ_e) at 1200 UTC correlates highest with snowfall at AWS3 (shown below). In the following paragraphs, the

variability of the background flow in the three moisture classes is discussed, based on the EOF pattern of θ_e .

The θ_e profiles in each class are characterized by the presence of potential instability (Figure 5, row 1). It is apparent, though, that snowfall events are associated with a potentially more unstable background flow than dry events. Table I substantiates this through the potential instability strength ($\Delta\theta_e$), obtained as the difference between the surface value and the minimum value in the θ_e sounding. In the DRY class, many profiles show a potentially stable layer below 600 hPa (either 825–700 or 700–600 hPa). These layers are discussed further in section 4.3.

The three leading modes of variability in the θ_e profiles are depicted in row 2 of Figure 5. For the two snowfall classes, EOF1 is dominant and explains more than 80% of the total variance. EOF1 variability is primarily expressed in the atmospheric boundary layer (ABL) where the highest loadings occur. In the DRY class, EOF2 is relatively more important than in the other classes, which indicates that variability in the 700–600 hPa layer does play a role for the total variance of θ_e during dry events.

To get a sense of the range of conditions (temperature and moisture structure) in the background flow for each class, we pick out the minimum and maximum in the EOF1 time series of θ_e . The two profiles selected this way are emphasized in Figure 5, row 1, and associated temperature and humidity profiles are shown in rows 3 and 4. Differences in temperature are very small and appear more clearly if temperature is expressed as static stability of the air column, here through the dry Brunt–Väisälä frequency (N_d) (Figure 5, row 3). However, static stability differences in the background flow must be much larger (by roughly one order of magnitude) to induce distinct flow regimes that lead to differing precipitation processes (see examples in Rotunno and Houze, 2007). The similarity of the N_d profiles (Figure 5) underlines the homogeneity of air temperature in the tropical climate on time-scales greater than intradiurnal (section 3.1; Kaser and Osmaston, 2002), and implies that variability in the θ_e profiles is essentially due to differences in the moisture content. Row 4 of Figure 5 confirms this notion. The relative position of the two specific humidity (q) profiles to each other – in each class – mimics the relative position of the two associated θ_e profiles (Figure 5, row 1).

For significant snowfall events, the data suggests that q near the surface must be $\geq 15 \text{ g kg}^{-1}$, and q at 500 hPa (q_{500}) $\sim 4 \text{ g kg}^{-1}$. Also typical during significant events is the peak in relative humidity (RH) close to the level of Kibo's summit (500 hPa). Normal snowfall events show a wider spread in possible moisture structures. It appears they can occur in response to any conditions between a relatively high (low) surface q but relatively low (high) q_{500} . The dominant background flow during DRY events shows a clear contrast to the snowfall classes, and has both a relatively small surface q ($< 12.5 \text{ g kg}^{-1}$) and q_{500} as well as $q_{600} \leq 2.5 \text{ g kg}^{-1}$. Relatively high moisture availability in the ABL thus appears to be the

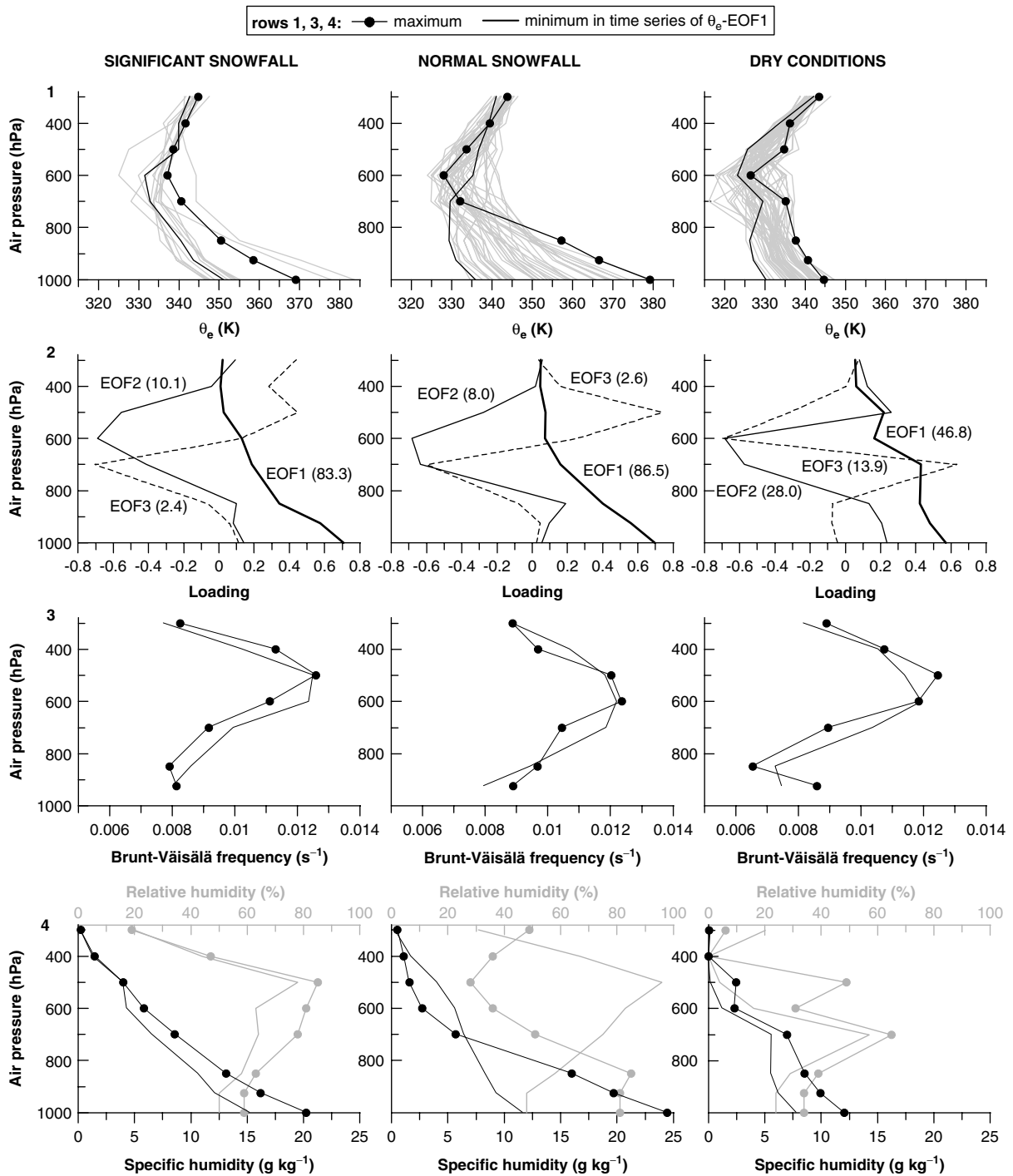


Figure 5. Vertical profiles in the background flow at 1200 UTC (reanalysis grid point 2.5° S/37.5° E) of (row 1) equivalent potential temperature (θ_e), (row 2) the three leading EOFs of θ_e variability (with percentages of explained variance in parentheses), (row 3) static stability, and (row 4) specific and relative humidity during (left) significant snowfall, (centre) normal snowfall, and (right) very dry conditions on Kibo's summit. Row 1 shows all profiles, rows 3 and 4 only the two profiles according to the minimum and maximum in the θ_e -EOF1 time series.

most reliable ingredient for snowfall on Kibo's summit, but a low q in the ABL can also result in summit snowfall if q in the mid troposphere is relatively high.

Two further issues deserve discussion in this section. First, and this concerns the SIG class, we find a strong correlation between the time series of θ_e -EOF2 and daily snowfall amount at AWS3 ($r = 0.63$). This correlation is even higher for the θ_e -EOF2 time series of the 0600 UTC profiles with $r = 0.73$. EOFs at 0600 UTC show a

pattern very similar to 1200 UTC (Figure 5, row 2), and a similar eigenvalue distribution as well (EOF1: 69%, EOF2: 19%). However, the dominant EOF1 is related slightly better to snowfall for 1200 UTC ($r = 0.3$) than for 0600 UTC ($r = 0.23$), which supports focusing on the 1200 UTC profiles in this study. EOF2 has its highest loadings around 600 hPa (Figure 5, row2, left panel), and correlations higher than 0.5 between q and daily snowfall indeed appear at 700, 600 and 500 hPa only (0.75, 0.63

and 0.56, respectively). This suggests that – once the preconditions for a SIG event are provided (a surface $q \geq 15 \text{ g kg}^{-1}$ and $q_{500} \approx 4 \text{ g kg}^{-1}$) – the actual snowfall amount on Kibo's summit strongly depends on the moisture content in the 700–500 hPa layer of the impinging flow.

Second, concerning all conditions, a further clear daily correlation between local snowfall and grid-box humidity or other useful precipitation proxies for the Tropics like top-of-atmosphere outgoing long-wave radiation (TOA-OLR) (e.g. Garreaud *et al.*, 2003) is not detectable in our data. This suggests that moist convection triggered by the isolated mountain has an important local effect on the interdiurnal variability of snowfall in the high-elevation zones. On a monthly scale, however, correlations improve in particular for TOA-OLR vs. snowfall ($r = -0.76$). This improvement for the longer time-scale could partly reflect the occasional contribution of large-scale organized convective systems to Kilimanjaro snowfall (Chan *et al.*, 2008), which are probably represented well in the grid-box value.

4.3. Simulated precipitation in different moisture classes

4.3.1. Input data

Building on the analysis in section 4.2, two basic experiments with the mesoscale model are conducted for each snowfall class, which reflect the respective range of θ_e variability. Hence, temperature (i.e. N_d) and humidity profiles shown in rows 3 and 4 of Figure 5 (left and centre) are used as input for the model runs. In order to further assess the most characteristic differences in these q profiles, the soundings at Nairobi are used as a comparison (Figure 6) from the Integrated Global Radiosonde Archive (Durre *et al.*, 2006). This is done at a 12-hour time-lag relative to Figure 5, when the soundings are archived (daily for 0000 UTC) and, importantly, the q profiles in the REA still show the same basic structure as in Figure 5 at 1200 UTC. Radiosonde data also suggest that the maximum case in the SIG class maintains a higher q than the minimum case over the ABL and most of the free troposphere, and the maximum case in the NORM class shows a higher q in the ABL but no more above ~ 700 hPa (Figure 6). Thus, the characteristic differences in the q structure between the two REA profiles of a snowfall class appear to be reliable. Table II summarizes the basic precipitation experiments and their nomenclature. A fifth experiment is presented for the DRY class ('DRY-moist 700' in Table II), where the second most important mode of θ_e variability (EOF2) refers to the tropospheric layer between 700 and 600 hPa (Figure 7). The one case with an almost saturated layer at 700 hPa ($RH = 93\%$) and a slightly stable layer below also leads to precipitation in the model on Kilimanjaro's slopes.

Profiles of wind speed and direction are also required as model input. While they do show differences in vertical wind shear among the experiments (Table II), an analysis

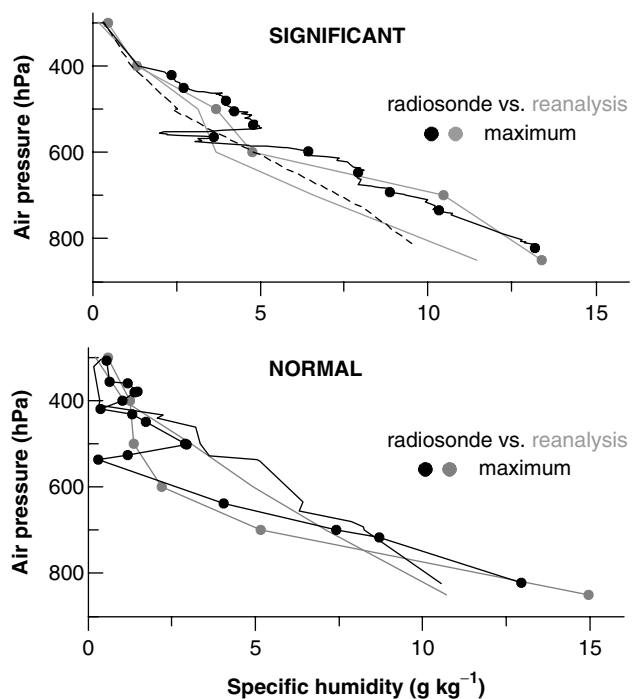


Figure 6. Vertical profiles of specific humidity in the background flow from the radiosonde at Nairobi ($1.3^{\circ}\text{S}/36.9^{\circ}\text{E}$, 820 hPa) and the reanalysis ($2.5^{\circ}\text{S}/37.5^{\circ}\text{E}$) at 0000 UTC on the day following the maximum and minimum in the 1200 UTC θ_e -EOF1 time series for snowfall classes (Figure 5). The dashed radiosonde case (minimum of 'significant' class) has missing data in the 700–550 hPa layer.

of wind profiles does not reveal any systematic differences between or within the classes. It is thus unlikely that particular directional and/or velocity shear patterns govern the weather of the three classes. The impact of wind shear on the simulated precipitation pattern is nonetheless examined later (section 4.3.3). Figure 8 shows that precipitation events on Kibo's summit are generally tied to easterly directions in the background flow, with a dominance of southeast in the ABL and east in the free troposphere. Hence, the larger-scale moisture influx from the east driven by synoptic-scale processes (Chan *et al.*, 2008) clearly affects Kilimanjaro (Figure 8).

4.3.2. Vertical pattern of precipitation

Figure 9 shows the simulated precipitation by means of scatter plots. Most notably, SIG events produce the largest precipitation rates at higher elevations than the other events. Experiment DRY-moist700 exhibits moderate and localized precipitation at mid elevations but cloud-free weather in the summit zone (discussed further in section 4.4). The heaviest precipitation falls in experiment NORM-max around 2000 m (on the southwestern slope), which corresponds to the forest zone. We experienced such a heavy event in the forest on 30 January 2005, and the moisture profile at 1200 UTC on that day (with a sharp decline from 12 to 4 g kg^{-1} between 850 and 700 hPa) clearly resembles the one in Figure 5 for the NORM-max case. The most balanced distribution of strong precipitation occurs in SIG-max (Figure 9), where the inflow has a relatively large q (and thus $RH \geq 60\%$) up to 500 hPa (see Figure 5).

Table II. Precipitation experiments with the mesoscale model and their background flow characteristics.

Experiment	Characteristics
SIG-max	rel. high low-level q ($\sim 20 \text{ g kg}^{-1}$), $q_{500} \approx 4 \text{ g kg}^{-1}$, RH_{\max} at 500 hPa (85%), directional wind shear at 500 hPa (SW, N to NE below and E to SE above), $F_m = 0.072$
SIG-min	rel. small low-level q ($\sim 15 \text{ g kg}^{-1}$), $q_{500} \approx 4 \text{ g kg}^{-1}$, RH_{\max} at 500 hPa (78%), little wind shear (inflow from NNE to NE at $3\text{--}5 \text{ m s}^{-1}$), $F_m = 0.088$
NORM-max	rel. high low-level q ($\sim 25 \text{ g kg}^{-1}$) but small q_{500} ($\sim 2 \text{ g kg}^{-1}$), low-level RH_{\max} (85%), inflow from SE but from NW to N in 700–500 hPa layer, $F_m = 0.078$
NORM-min	rel. small low-level q ($\sim 12 \text{ g kg}^{-1}$) but high q_{500} ($\sim 5 \text{ g kg}^{-1}$), RH_{\max} (96%) at 500 hPa, rather constant inflow ($5\text{--}7 \text{ m s}^{-1}$) from SE ($\geq 700 \text{ hPa}$) and NW to N ($< 700 \text{ hPa}$), $F_m = 0.085$
DRY-moist700	rel. high q_{700} ($\sim 8 \text{ g kg}^{-1}$), $q_{500} \approx 1 \text{ g kg}^{-1}$, stable layer 850–700 hPa, neutral layer 700–600 hPa, RH_{\max} (93%) and directional wind shear (W) at 700 hPa (else inflow from SE), $F_m = 0.068$

Flow characteristics are in terms of potential stability at low levels (700 hPa and lower), specific humidity (q) and relative humidity (RH) at various pressure levels (subscripts), winds (300 hPa and lower levels), and the unsaturated moist Froude number (F_m) estimated between surface and 500 hPa after Chen and Lin (2005) (and discussed further in section 4.4). ‘Relatively’ (rel.) refers to a moisture class, subscript ‘max’ denotes maximum. In the experiment names, ‘max’ and ‘min’ essentially indicate maximum and minimum low-level q , respectively, in the moisture class.

The lower right-hand plot of Figure 9 summarizes the vertical patterns by picking out the maximum P_r from each elevation band, and illustrates that the zone of maximum P_r moves upslope when precipitation on Kilimanjaro’s summit is significant. The more frequent NORM events have the greatest P_r around 2000–2500 m, which coincides with the zone of observed maximum annual precipitation (Røhr and Killingtveit, 2003; Hemp, 2006). The summary plot also provides an important basis for interpreting the observed seasonal precipitation variability at low and high altitude. The largest differences in P_r between SIG and NORM events occur at the highest altitudes, by a factor of ~ 4 above 4500 m, in Figure 9 (bottom right). Therefore, if SIG events are anomalously frequent (e.g. OND 2006) or fail in a wet season (e.g. OND 2005), the deviation relative to the temporal mean must be greater in the dry summit zone than in the moister lowlands – which is evident in the observations

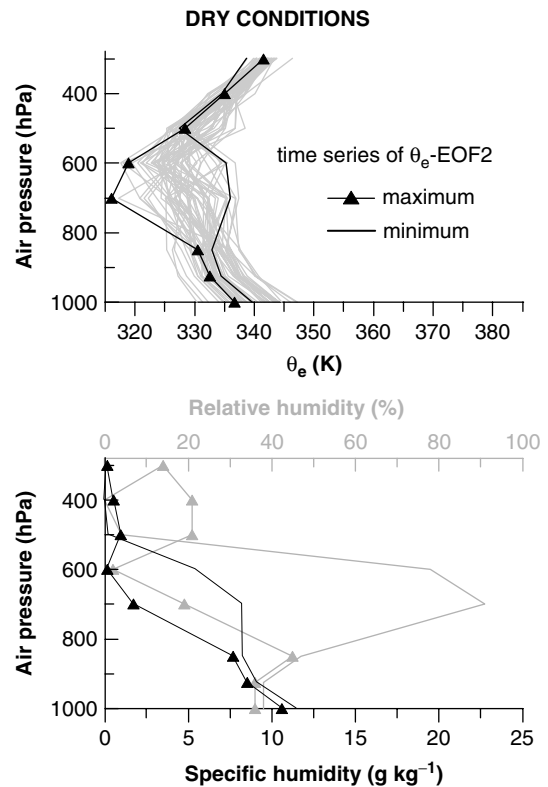


Figure 7. Vertical profiles in the background flow at 1200 UTC (reanalysis grid point $2.5^\circ\text{S}/37.5^\circ\text{E}$) of equivalent potential temperature (θ_e), specific and relative humidity during very dry conditions on Kibo’s summit. Profiles for the latter two are from the two days with the extreme values in the θ_e -EOF2 time series (emphasized in the θ_e plot).

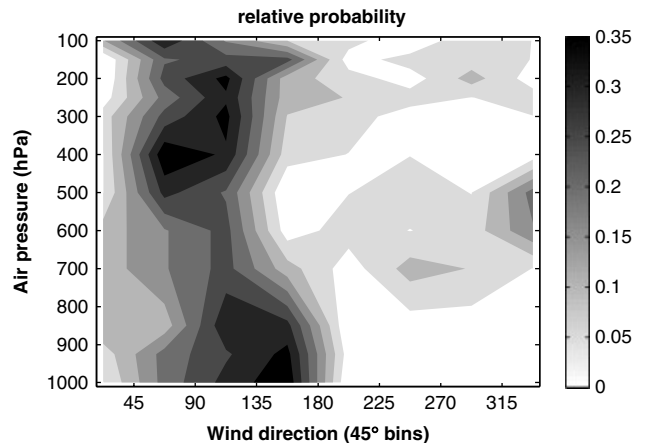


Figure 8. Relative probability of wind direction (45° bins, from north) between 1000 and 100 hPa in the background flow at 1200 UTC (reanalysis grid point $2.5^\circ\text{S}/37.5^\circ\text{E}$) for the ‘normal’ (NORM) snowfall class.

of Figure 4. Probably the smallest deviations occur in the moistest zone between *ca.* 1500 and 3000 m, where both SIG and NORM cases induce abundant precipitation, and moderate rain may even fall from air masses that cause dry weather on the summit and in the lowlands.

Observations of the vertical profile of precipitation on Kilimanjaro are not available at a high enough temporal resolution (see Tab. II in Røhr and Killingtveit, 2003) to validate the model result of an upslope shift in the zone

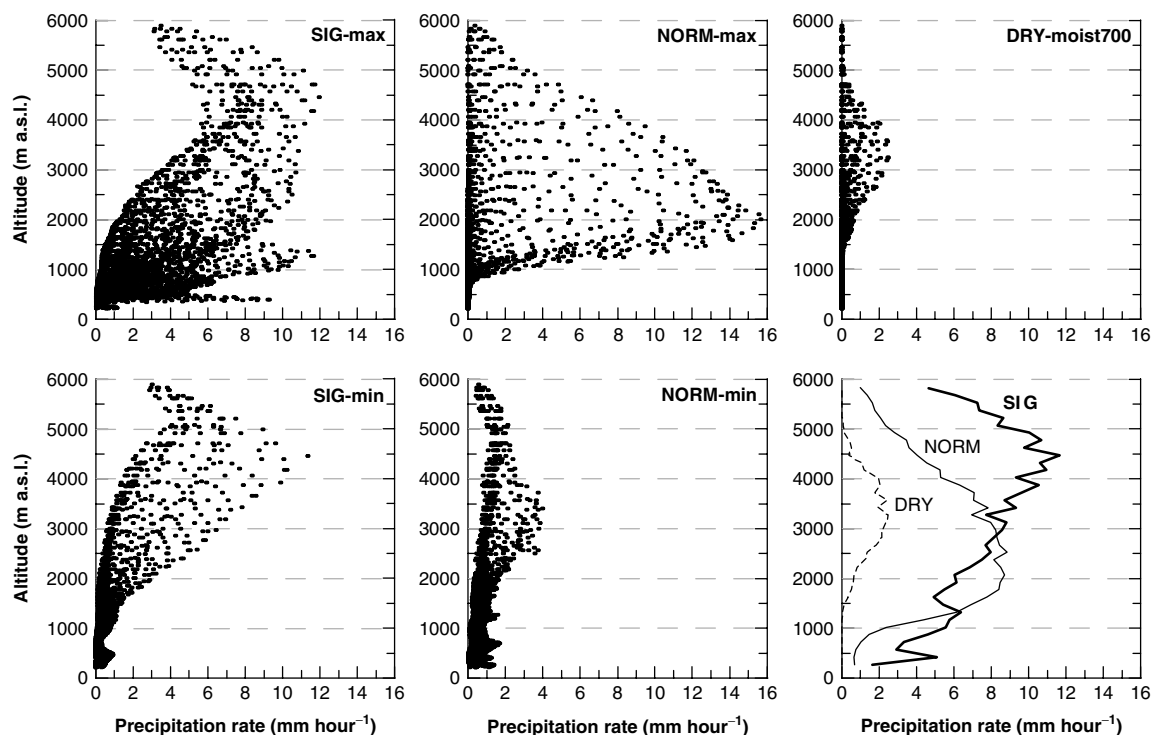


Figure 9. Simulated mean precipitation rate ($t = 3-5$ hours) versus altitude over the Kilimanjaro region (5184 grid points) in the precipitation experiments. The lower right-hand plot shows the maximum rate for elevation bands of 150 m (SIG and NORM curves averaged for 'max' and 'min' cases).

of maximum P_r when air masses get moister. However, Hastenrath (1984, 2005) has carefully compiled monthly precipitation at two different elevations on Mount Kenya ($0.2^\circ\text{S}/37.3^\circ\text{E}$) between 1978 and 1995: at 3050 m at the upper limit of the zone of maximum precipitation, and at 4200 m roughly 900 m below the summit (Hastenrath, 1984). These data help us to evaluate our model results and interpretations further, since anomalies in OND precipitation over equatorial East Africa similar to 2005 and 2006 occurred in 1982 and 1993 (Figure 10), and Mount Kenya lies in the same climatic regime as Kilimanjaro (Kaser and Osmaston, 2002). In the dry OND 1993, the climatological monthly mean precipitation was only slightly exceeded at 3050 m (which is weak for a wet season) but 40% less than the monthly mean fell at 4200 m (Figure 10, right). In the anomalously wet OND season of 1982 both elevations saw well above normal precipitation, which is amplified in relative terms at the

more elevated site. The number of significant events at 4200 m was also appreciably larger in 1982 than in 1993. The measurements from Mount Kenya thus support the pattern modelled for Kilimanjaro: an upslope shift of the zone with maximum P_r during significant precipitation events on equatorial mountains, and greater percentage deviations from the mean at high (and dry) elevation zones than at mid and low (moist) elevation zones when wet seasons experience anomalous frequencies of these events.

4.3.3. Sensitivity tests

The main result presented above (vertical shift of maximum P_r between SIG and NORM events) is generally robust, as evaluated from the numerous preliminary runs that we conducted while establishing the final model set-up. Table III elaborates on the sensitivity of the result

Table III. Elevation difference of the grid points with maximum precipitation (Δz_{pmax}) between experiments SIG-min and NORM-max over the Kilimanjaro region.

Change in set-up	Δz_{pmax} (m)	P_r (mm hour $^{-1}$)
none: reference runs (Table II)	2461	11.3
no wind shear	2607	7.0
$\Delta T_{dsa} = +0.25$ K	2461	13.1
$\Delta T_{dsa} = +0.5$ K	2691	17.0
warm-water microphysics	1962	4.1

For reference run; after removing wind shear in the background flow (5 m s^{-1} from east for both experiments); and after changing the lower boundary condition (surface heating) and precipitation microphysics. The maximum mean precipitation rate ($t = 3-5$ hours) in experiment SIG-min is also given.

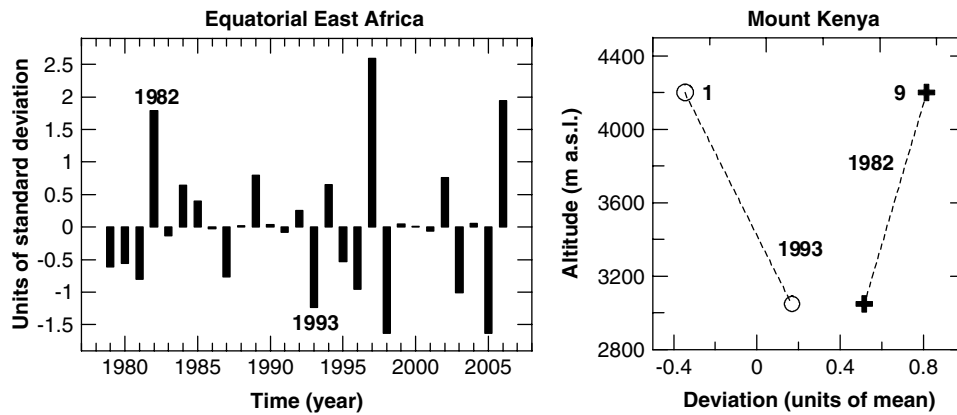


Figure 10. Standardized and area-averaged OND precipitation in equatorial East Africa ($28.75\text{--}38.75^\circ\text{E}$, $3.75^\circ\text{N}\text{--}3.75^\circ\text{S}$) from the satellite-based CMAP observations (Xie and Arkin, 1997) between 1979 and 2006, and OND precipitation variability (deviation in units of monthly mean per month, 1978–1995) at two elevations on Mount Kenya in 1982 and 1993 from monthly rain gauge observations (compiled by Hastenrath, 1984, 2005). The number for the high site gives daily significant events with a daily sum $\geq +2\sigma$ (data provided by the Kenya Meteorological Department).

to the two most vital aspects: (1) Is the assumption that differing wind shear patterns do not govern the weather of the different classes (section 4.3.1), and thus the altitude dependency of precipitation, reasonable, and (2) Do small variations in the imposed surface-to-air temperature difference (T_{dsa}) change the main result? Experiments SIG-min and NORM-max are considered in Table III, since they show the vertical difference in the zone of maximum P_r (ZMP) particularly well (see Figure 9). The differing wind conditions in the background flow do indeed not explain the altitude difference in the ZMP (Table III). Setting $T_{\text{dsa}} = 1\text{ K}$ reproduces observed P_r on the summit well (see section 3.3), but may also incorporate other uncertainties. Changing the tuning parameter T_{dsa} should therefore only alter the magnitude of P_r but not the locations of precipitation zones – which is the case in Table III. In all mentioned runs, the elevation difference in the ZMP amounts to roughly 2400–2700 m (Table III). The experiment in the last line of Table III is discussed in section 4.4.2.

4.4. Causal factors of the precipitation distribution

4.4.1. The downstream precipitation maximum

Kilimanjaro should in general experience the ‘flow-around’ regime due to its enormous height and the resultant dimensionless mountain height, M (also known as inverse Froude number), clearly exceeding 1 (Schär, 2002). This means that impinging air masses are typically blocked, undergoing flow splitting and lateral deflection on the windward side. The effects of flow blocking on orographic precipitation have been examined in many studies (see Roe, 2005), and underlying mechanisms can differ substantially from those of ‘flow-over’ cases (e.g. Jiang, 2003).

Figure 11 illustrates the mesoscale circulation in experiment SIG-min where the inflow up to the mountain peak comes rather uniformly from north to northeast (Table II). Noteworthy features are: (1) On the windward side, the incoming flow is blocked and deflected around

the mountain. Flow stagnation (‘stagnation point’) occurs at $\sim 3200\text{ m a.s.l.}$, above which a counterflow evolves. (2) After the incoming flow has circumscribed the mountain, two eddies are formed in the lee of the mountain with centres roughly at $x = 80\text{ km}$ and $y = -108\text{ km}$, and $x = 106\text{ km}$ and $y = -122\text{ km}$. (3) Between the pair of eddies, flow reversal occurs in a broad zone over the southern and southwestern mountain slopes. (4) Two belts of ascending air are present. The lower-lying belt connects ascending air on the windward slopes with that in the lee-side zone of flow reversal. The upper belt encloses the area just below the summit and marks the upper end of the stagnation zone beneath (e.g. Jiang, 2003). (5) On the peak, characteristic northeasterly winds occur (at 5895 m from 32°), which differ less from the background flow (inflow at 500 hPa is from 23°) than the winds over the slopes controlled by mountain-induced circulation. Similar features and implications of windward flow blocking are evident in the other experiments, which is not surprising in light of the very small moist Froude numbers in all experiments (Table II).

The simulated circulation, with flow reversal and convergence zones in the lee of the mountain, shifts a significant fraction of precipitation to the lee-side slopes (Figure 11). This also helps to better understand observations on Kilimanjaro, since the background flow is mostly easterly (Figure 8) but the climatological precipitation maximum is found on the southwesterly flanks (Coultts, 1969; Hemp, 2006). Already Klute (1916) noted that ‘moist air ascends on the southern flanks of Kilimanjaro’, which likely refers to a zone of flow reversal. Geilinger (1936) wrote that easterly flows toward the mountain seem to cause a counterflow on the southwestern side of Kilimanjaro, which transports moisture from the lowlands uphill – a situation that does appear in Figure 11.

Apart from the characteristics of the mesoscale flow, the type of precipitation formed is also important to our discussion. The production time for convective precipitation is greater than for stratiform precipitation, so convection is a major factor for shifting the precipitation

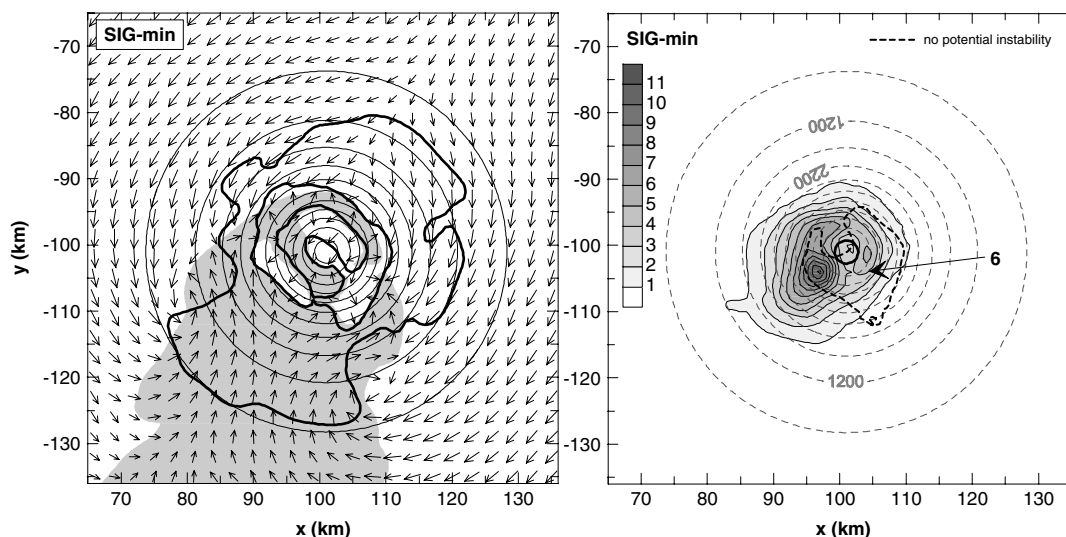


Figure 11. (left) Mesoscale circulation at $t = 3$ hours in experiment SIG-min (inflow from northeast): wind vectors at the surface with grey shading denoting a positive v -component (i.e. towards north), and bold lines delineating the areas of the w -component $\geq 0.1 \text{ m s}^{-1}$ at the surface (i.e. air ascent). (right) Mean precipitation rate (mm hour^{-1}) from $t = 3\text{--}5$ hours as filled contours. The dashed black line delineates the area $> 1 \text{ mm h}^{-1}$ in a sensitivity run with neutral upstream stability (see text), where the number and arrow give amount and location of the maximum. The topography of the mountain is depicted by the circles (500 m spacing), with the summit area (5700 m contour) highlighted by the bold black contour in the right-hand plot.

signal downstream (Fuhrer and Schär, 2005). For example, Jiang (2003) shows precipitation on the windward slope of an isolated bell-shaped mountain in flow-around experiments with stable upslope ascent. Evidence of convection on Kilimanjaro has been shown in Table I, where precipitation events on the summit coincide with low horizontal wind speeds. Table IV lists further statistics and substantiates the convective nature of precipitation on Kilimanjaro. Isolated updraughts and downdraughts are well developed (with a very similar magnitude in runs using $\Delta x = \Delta y = 500 \text{ m}$), and precipitation on Kilimanjaro typically falls from statically unstable clouds ($N_m^2 < 0$). The latter is calculated by the squared moist buoyancy frequency N_m^2 for the cloud regions (Jiang, 2003; Kirshbaum and Durran, 2004), which is analogous to N_d but for a saturated environment. Further evidence of convection is found in the simulated hydrometeors that contain a significant portion of graupel (detailed in section 4.4.2), which is in agreement with our observations (see section 3.2).

To investigate the importance of convective dynamics we consider results from a sensitivity run, where potential instability in the SIG-min background flow is removed by decreasing air temperature at low levels (e.g. Fuhrer and Schär, 2005). Thus θ_e at 1000, 925 and 850 hPa is reduced to 335 K (cf. Figure 5, top left, for the initial unstable profile). This change does not alter the general flow regime, since $M = 1/F_m$ (based on F_m as computed in Table II) remains almost unchanged (> 10), and items (1)–(5) above also appear in this run. Precipitation intensity and area, however, decrease, and the latter is concentrated on the windward eastern flanks of the mountain (Figure 11, right). Thus the development of convection – for an unchanged flow regime – appears to be key in controlling the observed downstream precipitation maximum on Kilimanjaro. The circulation patterns

due to flow-blocking provide an amplifying factor by promoting upslope moisture transport in the lee of the mountain.

It is not unusual in other geographic regions for atmospheric flows to detour around mountains and precipitation to spread above recirculating wake regions in the lee of them (e.g. Roe, 2005). Precipitation and convection on tropical mountains are, however, often linked to the diurnal cycle of insolation: the strong sun heats the slopes during the course of a day, which leads to cloud formation and precipitation primarily on western slopes that face the afternoon sun (Troll and Wien, 1949; Hastenrath, 1991). Our intention is not to exclude the possibility that this occurs, but we feel that it is important to demonstrate (see above) that precipitation patterns on free-standing tropical mountains – and associated convection due to orographic lifting – can also have a mesoscale dynamical component (as differential surface heating is not resolved in our experiments).

4.4.2. The altitude of the precipitation maximum

The occurrence of maximum P_r at mid elevations is a direct manifestation of precipitation formation through convective dynamics (Hastenrath, 1991). To help identify processes that control the actual altitude of maximum P_r , Table IV shows three-dimensional latent heating in the cloud region and air mass ascent. The combination of high static instability and strong latent heating in the cloud for SIG cases is systematically tied to more air ascent (Table IV). The particular case DRY-moist700 shows high static instabilities because of a relatively large vertical gradient in the total water mixing ratio (due to a sharp transition between cloud and cloud-free layers; discussed below), but little latent heating and air ascent. Figure 12 extends to the spatial distribution of the

Table IV. Domain extremes of vertical velocity (w , updraughts and downdraughts) from $t = 3-5$ hours in the precipitation experiments for the Kilimanjaro region. Also, maximum and minimum of the squared moist buoyancy frequency (N_m^2), the 90% percentiles of latent heat in the cloud (LH_{90}) and of vertical velocity (w_{90}) at $t = 4$ hours.

Experiment	w ($m\ s^{-1}$)	N_m^2 ($10^{-4}\ s^{-2}$)	LH_{90} ($W\ m^{-3}$)	w_{90} ($m\ s^{-1}$)
SIG-max	5.9/−2.3	−0.9/−8.3	1.3	0.34
SIG-min	2.9/−3.2	−1.2/−8.1	1.1	0.26
NORM-max	6.7/−2.4	−1.0/−7.7	0.7	0.08
NORM-min	3.6/−3.5	0.3/−7.2	0.9	0.18
DRY-moist700	1.6/−1.6	−1.6/−8.1	0.5	0.16

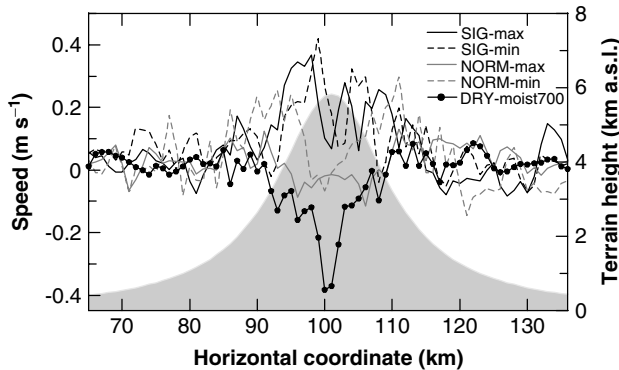


Figure 12. Mass-weighted vertical velocity averaged between surface and 400 hPa (~ 8 km) and for $t = 3, 4$ and 5 hours along the domain centre through the mountain peak (mean from W–E and N–S sections) in the precipitation experiments. The terrain is shown for reference as filled plot.

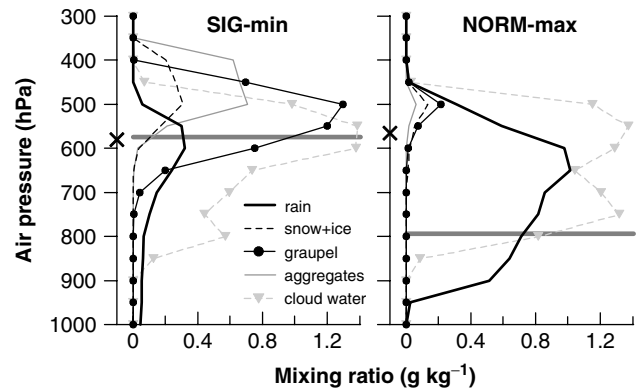


Figure 13. Maximum mixing ratios of rain, snow plus pristine ice, graupel, aggregates and cloud water versus binned air pressure (bin size is 50 hPa) in experiments SIG-min and NORM-max at $t = 4$ hours. The horizontal grey line indicates the altitude of the precipitation maximum on the mountain slope, and the cross on the y -axis the $0^\circ C$ isothermal surface.

vertically-averaged motion, which is computed with the method of Colle (2008). The most prominent differences are found for high-elevation terrain above 4000 m a.s.l., where SIG cases coincide with the maximum air lifting, NORM cases approximate zero, and subsidence exists in the DRY case. This result is maintained if only W–E or N–S sections are plotted. The analyses thus suggest that stronger air ascent during SIG events, particularly over the higher-elevation slopes, (1) favours the upslope transport of moisture from lower elevations, and (2) therefore creates the basis for efficient precipitation growth over the high-elevation terrain – which ultimately causes the high-altitude maximum of precipitation.

Microphysical processes in clouds exert the second major impact on orographic precipitation besides dynamical factors and, as indicated above by items (1) and (2) as well as in section 4.4.1, both are not independent of each other (Rotunno and Houze, 2007). Figure 13 targets again experiments SIG-min and NORM-max with their well-developed altitude difference in the precipitation maximum, and shows the vertical hydrometeor distribution. The maximum values are plotted, because there is a clear spatial coherence in the horizontally projected distributions of precipitation and vertically integrated condensate (not shown). The precipitable hydrometeor species are dominated by rain in NORM-max, while graupel prevails in SIG-min (Figure 13). The latter as well as other solid hydrometeors (snow, ice, aggregates) peak at upper

levels where cloud water is being depleted, which suggests that solid particles grow at the expense of cloud droplets due to riming. Solid precipitation is thus formed at levels in the vicinity of the mountain summit during SIG events, which is evident in Figure 14 for graupel and leads to a short hydrometeor residence time (and hence a great microphysical efficiency) over high-elevation terrain. The maximum of rain in NORM-max develops in lower layers where cloud water decreases sharply from its low-level maximum (Figure 13), which indicates a region of significant collision and coalescence of cloud droplets. These processes – which can be viewed as the warm cloud equivalent of the upper-level riming in terms of efficiency (Rotunno and Houze, 2007) – induce a fast precipitation growth at low levels and lead to the precipitation maximum directly beneath at ~ 800 hPa (Figure 13). The altitude characteristics of microphysical efficiency, and thus the elevation difference in maximum P_r , are maintained if only warm-water physics are allowed in the two runs (Table III). Although precipitation intensity decreases, the SIG simulation maintains the higher-elevation maximum P_r (Table III). This suggests that mixed-phase precipitation physics are a driver, but not the main control, of the modelled altitude dependency of precipitation.

Similar to SIG events, minor precipitation events (NORM-min and DRY-moist700) show an upper-level maximum of RH in the background flow (see Figure 5)

but fail to produce high graupel amounts at and above summit levels, which keeps microphysical efficiency over high-elevation terrain small (Figure 14). This failure likely originates from the relatively small humidity in the ABL of the background flow, which constrains the strength of feedback between air lifting and microphysical processes (condensation) through the effect of latent heat (e.g. Table IV, Figure 14). On the other hand, a high moisture content in the ABL alone (experiment NORM-max) cannot cause a high-elevation maximum of P_r either, since precipitation growth mostly occurs at low levels (Figure 13) and vertical transport of moisture to high elevations is insufficient (Figure 12). Thus, the factors controlling the altitude dependency of precipitation can be tied back largely to the input humidity profile.

The total condensate distribution (Figure 14) further exhibits that the clouds ‘sit’ on the mountain in SIG and NORM experiments, which is often observed over Kilimanjaro and has been well documented by photography. Of particular interest is the cloud pattern in experiment DRY-moist700 (a simulation for the JJAS dry season), which fails to close over the mountain peak and remains stratiform (Figure 14). We have observed this pattern frequently during our dry-season field trips, and it has been described as one characteristic feature of cloud formation on Kilimanjaro (Kaser and Osmaston, 2002). Thus, the presence of a moist and potentially slightly stable or near-neutral layer between 800 and 600 hPa in the background flow (Figure 7), and resultant subsidence over the peak (Figure 12), rank as possible causes of this phenomenon.

5. Discussion: a climatology context

There is convincing evidence that precipitation variability and changes in the Tropics over a defined time period result primarily from changes in the number of wet and dry episodes (frequency) within that period, rather than from unprecedented precipitation amounts per episode. This applies to the intraseasonal and interannual time-scales where episodes are days and seasons (Garreaud *et al.*, 2003), but also to climatological scales where episodes may be years or decades (Nicholson, 2000; Hastenrath, 2001; Mölg *et al.*, 2006). Measurements from Kibo’s summit demonstrate this nicely. The wettest season, OND 2006, does not feature atypical snowfall amounts but just a more frequent occurrence of wet days (Figure 2, Figure 4). The opposite effect is seen for the anomalously dry OND 2005 season with a high frequency of dry days (Figure 4). In light of the simulated precipitation profiles (Figure 9), this suggests that (1) moisture changes over tropical high mountains – also beyond the seasonal time-scale – most probably coincide with a vertical shift of the mean elevation of maximum precipitation and, as a result, (2) the precipitation change relative to a longer-term mean is more drastic at high altitude than at mid and low elevations. As discussed in section 4, item (2) is evident in observations of seasonal variability (Figures 4 and 10).

For a further examination of these frequency changes in the tropical moisture climate, we turn to glacier recession on Kilimanjaro which is forced by a drier regional climate (see section 2). Any available time series of moisture should therefore indicate changes in the frequency of dry and wet episodes on Kibo’s summit, but not necessarily changes in snowfall amounts during wet days. REA

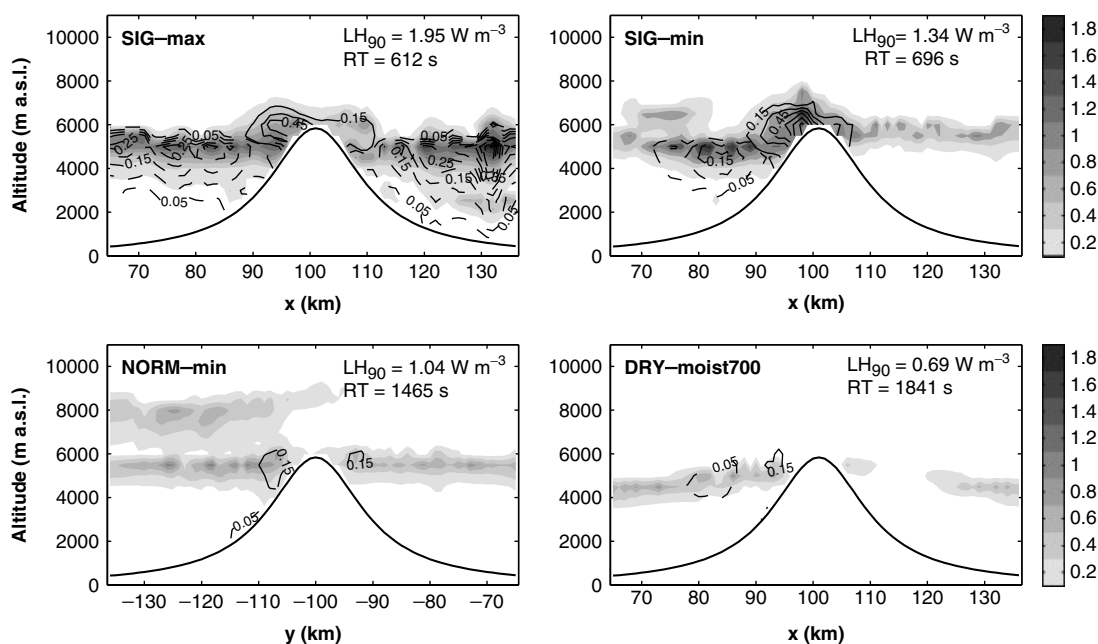


Figure 14. Vertical cross-sections through the domain centre (x -axis is west–east, y -axis is south–north) of mixing ratios of total condensate (filled contours, in g kg^{-1}), graupel (solid lines every 0.15 g kg^{-1}), and rain (dashed lines every 0.05 g kg^{-1}) at $t = 4$ hours in four of the basic experiments. LH₉₀ gives the 90% percentile of latent heat in the cross-section’s cloud. RT is the mean hydrometeor residence time over terrain >2500 m a.s.l., calculated after Colle (2008) (total condensate amount aloft/precipitation rate; both as means from $t = 3$ – 5 hours). The z -axis is vertically exaggerated.

are the only long-term data for the free troposphere over Kilimanjaro, and we fully appreciate that time series analysis with REA may be problematic due to modifications in the assimilation process (Kistler *et al.*, 2001). To limit this issue, only data after the introduction of satellite observations are considered here. This time period is sufficiently long, since glacier shrinkage on Kibo between the late 1970s and the present has been clearly detectable (Cullen *et al.*, 2006). Moreover, we perform this time series analysis using the composite of different variables associated with precipitation, and different pressure levels, which supports robustness of the results.

Figure 15 estimates the number of potential SIG and DRY events from 1979 to 2006, by using moisture thresholds at different pressure levels as discussed in sections 4.2 and 4.3 (see also caption of Figure 15). For snowfall in general, the potential instability strength in the background flow (Table I) is assessed with respect to a threshold of $\Delta\theta_e = 18$ K in Figure 15, based on the observation that the 70% percentile for DRY (17.9 K), the 30% percentile for NORM (17.6 K), and the 30% percentile of SIG events (18.3 K) converge at this value. On decadal time-scales, there is thus a high probability that the fluctuation around this threshold holds information on snowfall occurrence on Kibo's summit. Also shown in Figure 15 is specific humidity at 700 hPa, which is the best proxy for daily snowfall amount during SIG events (section 4.2).

The various time series together (Figure 15) give a consistent picture. Compared to the 1980s and early 1990s, the latter half of the examined period has seen a higher

frequency of dry episodes along with lower frequencies of snowfall conditions and significant snowfall events on Kibo's summit, and furthermore an increase in the potential stability of the atmospheric column. Year 2006 is the most prominent wet anomaly for the latter half of the period. The 700 hPa moisture for SIG cases, on the other hand, shows a negative tendency only from days 90 to 135 and does not suggest a longer-term change in daily precipitation amounts (Figure 15). The presented composite analysis adds further details to the issue of why moisture-sensitive phenomena like slope glaciers (Cullen *et al.*, 2006) and vegetation zones (Hemp, 2005) on Kilimanjaro have changed significantly between the 1980s and the present.

While the tropical atmosphere is generally expected to harbour more moisture under global warming (following Clausius–Clapeyron scaling), accompanying mechanisms can also decrease tropical precipitation on the regional scale, for instance a shift of the convective margin (Chou *et al.*, 2006; Lintner and Neelin, 2007). Such an inland shift cannot be ruled out for equatorial East Africa since the 1980s (Mölg *et al.*, 2009b), and is thus one possible forcing of the increased (decreased) number of dry (wet) spells detected in the background flow over Kilimanjaro (Figure 15). A more detailed discussion about 20th century climate change and its regional implications for East Africa is provided in Mölg *et al.* (2009b).

6. Conclusions

Air masses that approach Kilimanjaro on the daily scale (the background flow) are characterized by differences in

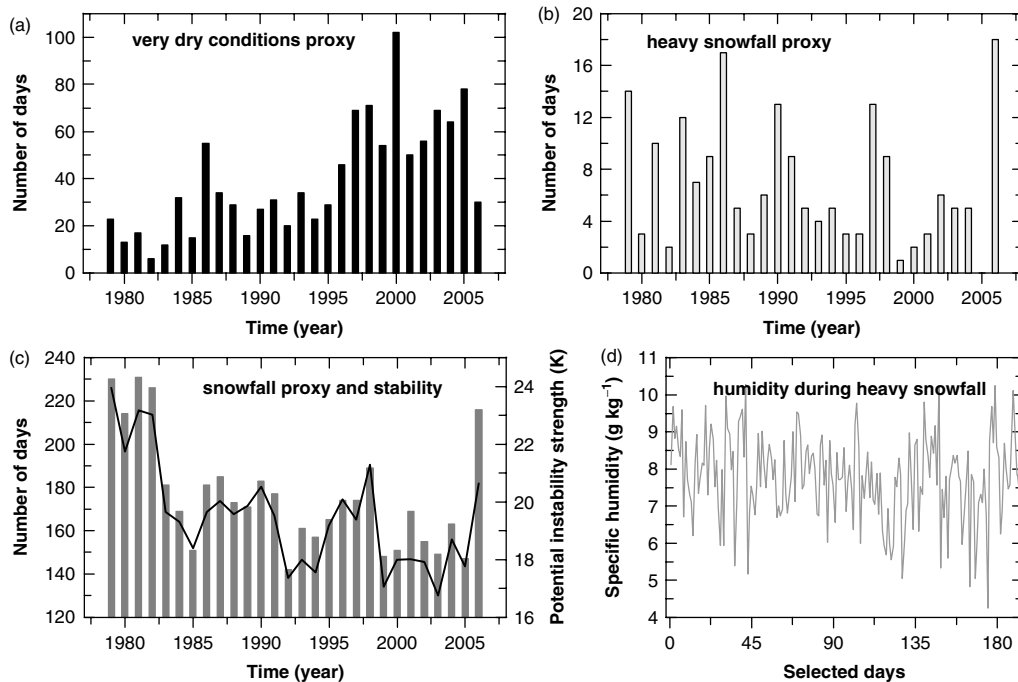


Figure 15. Annual number of days that show the potential of (a) very dry conditions ($q_{1000} < 12.5$ and q_{600} and $q_{500} < 2.5$ g kg⁻¹; $N = 1105$ days), (b) significant snowfall ($q_{1000} \geq 15$ and $q_{500} \geq 4$ g kg⁻¹; $N = 192$ days), and (c) high snowfall probability ($\Delta\theta_e > 18$ K, $N = 4932$ days, with mean annual $\Delta\theta_e$ also shown as the line plot) on Kibo's summit between 1979 and 2006 (evaluated from reanalysis grid point 2.5° S/37.5° E at 1200 UTC). (d) Specific humidity at 700 hPa during the selected 192 days of significant snowfall.

moisture content and potential instability, but much less by temperature differences. A high moisture content in the atmospheric boundary layer (ABL, $q > 15 \text{ g kg}^{-1}$) is one precondition for ‘significant’ precipitation events on Kilimanjaro’s summit. A second control is exerted by the moisture content in the 700–500 hPa layer, which determines precipitation amounts during the significant events or can lead to ‘normal’ precipitation events on the summit even if ABL humidity in the impinging flow is rather low ($\sim 12 \text{ g kg}^{-1}$).

Idealized simulations with an atmospheric model, using different background flow characteristics as forcing, demonstrate that the elevation zone of maximum precipitation is shifted upslope from $\sim 2000 \text{ m a.s.l.}$ during normal events to $\sim 4500 \text{ m a.s.l.}$ during significant events. Substantial differences in precipitation between such events therefore appear in the dry summit zone, while small differences occur in the moister mid- and low-elevation zones.

This modelled pattern of space–time variability is evident in observations of seasonal precipitation variability from the lowlands and the summit of Kilimanjaro ($\sim 5900 \text{ m a.s.l.}$) during anomalous wet seasons (OND 2005 and 2006), which are governed by anomalous frequencies of significant events. In these data, the deviation relative to the mean precipitation is increased at high elevation. The same applies to observations from two different elevation zones on nearby Mount Kenya during previous anomalous wet seasons.

Model simulations also suggest that convective dynamics shift the precipitation maximum to the leeward mountain flanks, where the climatological precipitation maximum is observed (Coutts, 1969; Hemp, 2006). Leeward precipitation is moreover favoured by the formation of lee-side flow reversal after lateral deflection of incoming air masses around the mountain. As the impinging air becomes moister, latent heating and static instabilities in clouds, air lifting over the slopes, and microphysical efficiency at high altitude are all increased – which shifts the precipitation maximum to high elevations during significant events.

Regional climate change and variability in the Tropics beyond the seasonal scale are also governed by frequency changes of dry- and moist-air advection (e.g. Nicholson, 2000; Hastenrath, 2001). Hence, the ‘belt’ of maximum precipitation on tropical mountains most probably migrates vertically under tropical climate change, and precipitation changes are most drastic in the dry high-elevation zones. In East Africa the decrease in wet episodes marked the transition from the late 19th century wet climate to the 20th century dry climate (Nicholson, 2000; Hastenrath, 2001; Mölg *et al.*, 2006, 2009b). A simple calculation of precipitation proxies between 1979 and 2006 suggests the regions around Kilimanjaro are still experiencing an increase (decrease) in the number of dry (wet) episodes. This agrees with the more recent observations of social (e.g. Mwangi and Desanker, 2007) and environmental implications of drought in East Africa (e.g. Hemp, 2005; Cullen *et al.*, 2006).

Acknowledgements

This study was funded by the Austrian Science Foundation (FWF, grants no. P-17415-N10, no. P-20089-N10), the Austrian-American Fulbright Programme, and the Tyrolean Science Foundation (TWF). It was also supported by the Austrian Ministry of Science (BMWF) as part of the ‘UniInfrastrukturprogramm’ of the ‘Forschungsplattform IAC’ at the LFU Innsbruck. JC was funded by a grant from the Comer Science and Education Foundation. Local support in Tanzania is provided by the Commission for Science and Technology (COSTECH), Kilimanjaro and Tanzania National Park Authorities (KINAPA and TANAPA), the Tanzania Meteorological Agency (TMA), and the Tanzania Wildlife Research Institute (TAWIRI). NCEP/NCAR reanalysis and CMAP data were obtained from the NOAA/OAR/ESRL PSD, Boulder, Colorado, USA, and TRMM data from the Goddard Distributed Active Archive Center. TRMM is an international project jointly sponsored by the Japan National Space Development Agency (NASDA) and the US National Aeronautics and Space Administration (NASA) Office of Earth Sciences. Daily precipitation data from Mount Kenya were provided by Charles Mutai from the Kenya Meteorological Department (KMD). Simulations with RAMS were conducted at the Central Information Technology Services (ZID) of the University of Innsbruck on the Linux cluster ZID-CC, which is maintained by Gerhard Niederwieser and his team. Comments of two reviewers and the editors improved this manuscript significantly. This paper is a contribution to both the ‘Climate and Cryosphere’ focus, and the ‘High Performance Computing’ focus at Innsbruck University.

References

- Bormann N, Marks CJ. 1999. Mesoscale rainfall forecasts over New Zealand during SALPEX96: Characterization and sensitivity studies. *Mon. Weather Rev.* **127**: 2880–2893.
- Chan RY, Vuille M, Hardy DR, Bradley RS. 2008. Intraseasonal precipitation variability on Kilimanjaro and the East African region and its relationship to the large-scale circulation. *Theor. Appl. Climatol.* **93**: 149–165.
- Chen S-H, Lin Y-L. 2005. Effects of moist Froude number and CAPE on a conditionally unstable flow over a mesoscale mountain ridge. *J. Atmos. Sci.* **62**: 331–350.
- Chiang JCH, Lintner BR. 2005. Mechanisms of remote tropical surface warming during El Niño. *J. Climate* **18**: 4130–4149.
- Chou C, Neelin JD, Tu J-Y, Chen C-T. 2006. Regional tropical precipitation change mechanisms in ECHAM4/OPYC3 under global warming. *J. Climate* **19**: 4207–4223.
- Clark CO, Webster PJ, Cole JE. 2003. Interdecadal variability of the relationship between the Indian Ocean zonal mode and East African coastal rainfall anomalies. *J. Climate* **16**: 548–554.
- Colle BA. 2008. Two-dimensional idealized simulations of the impact of multiple windward ridges on orographic precipitation. *J. Atmos. Sci.* **65**: 509–523.
- Cotton WR, Pielke Sr RA, Walko RL, Liston GE, Tremback CJ, Jiang H, McAnelly RL, Harrington JY, Nicholls ME, Carrio GG, McFadden JP. 2003. RAMS 2001: Current status and future directions. *Meteorol. Atmos. Phys.* **82**: 5–29.
- Coutts HH. 1969. Rainfall of the Kilimanjaro Area. *Weather* **24**: 66–69.
- Cullen NJ, Mölg T, Kaser G, Hussein K, Steffen K, Hardy DR. 2006. Kilimanjaro glaciers: Recent areal extent from satellite data and new interpretation of observed 20th century retreat rates. *Geophys. Res. Lett.* **33**: L16502, DOI: 10.1029/2006GL027084.
- Dettinger M, Redmond K, Cayan D. 2004. Winter orographic precipitation ratios in the Sierra Nevada – Large-scale atmospheric

- circulations and hydrologic consequences. *J. Hydrometeorol.* **5**: 1102–1116.
- Durre I, Vose RS, Wuertz DB. 2006. Overview of the Integrated Global Radiosonde Archive. *J. Climate* **19**: 53–68.
- Fuhrer O, Schär C. 2005. Embedded cellular convection in moist flow past topography. *J. Atmos. Sci.* **62**: 2810–2828.
- Garreaud R, Vuille M, Clement AC. 2003. The climate of the Altiplano: Observed current conditions and mechanisms of past changes. *Palaeogeogr. Palaeoclimatol. Palaeoecol.* **194**: 5–22.
- Geilinger W. 1936. The retreat of the Kilimanjaro glaciers. *Tanganyika Notes and Records* **2**: 7–20.
- Gohm A, Mayr GJ. 2005. Numerical and observational case-study of a deep Adriatic bora. *Q. J. R. Meteorol. Soc.* **131**: 1363–1392.
- Hardy DR. 2003. Kilimanjaro snow. In *State of the Climate in 2002*, Waple AM, Lawrimore JH (eds). *Bull. Am. Meteorol. Soc.* **84**: S48.
- Hastenrath S. 1984. *The glaciers of equatorial East Africa*. D. Reidel: Dordrecht, Boston, Lancaster.
- Hastenrath S. 1991. *Climate dynamics of the Tropics*. Kluwer: Dordrecht, Boston, London.
- Hastenrath S. 2001. Variations of East African climate during the past two centuries. *Clim. Change* **50**: 209–217.
- Hastenrath S. 2005. *Glaciological studies on Mount Kenya 1971–2005*. University of Wisconsin: Madison.
- Hastenrath S, Polzin D, Mutai C. 2007. Diagnosing the 2005 drought in equatorial East Africa. *J. Climate* **20**: 4628–4637.
- Hemp A. 2005. Climate change-driven forest fires marginalize the impact of ice cap wasting on Kilimanjaro. *Global Change Biol.* **11**: 1013–1023.
- Hemp A. 2006. Vegetation of Kilimanjaro: Hidden endemics and missing bamboo. *Afr. J. Ecol.* **44**: 305–328.
- Huffman GJ, Adler RF, Bolvin DT, Gu G, Nelkin EJ, Bowman KP, Hong Y, Stocker EF, Wolff DB. 2007. The TRMM Multisatellite Precipitation Analysis (TMPA): Quasi-global, multiyear, combined-sensor precipitation estimates at fine scales. *J. Hydrometeorol.* **8**: 38–55.
- Indeje M, Semazzi FHM, Ogallo LJ. 2000. ENSO signals in East African rainfall seasons. *Int. J. Climatol.* **20**: 19–46.
- Jiang Q. 2003. Moist dynamics and orographic precipitation. *Tellus* **55A**: 301–316.
- Kalnay E, Kanamitsu M, Kistler R, Collins W, Deaven D, Gandin L, Iredell M, Saha S, White G, Woollen J, Zhu Y, Leetmaa A, Reynolds R, Chelliah M, Ebisukaki W, Higgins W, Janowiak J, Mo KC, Ropelewski C, Wang J, Jenne R, Joseph D. 1996. The NCEP/NCAR 40-year reanalysis project. *Bull. Am. Meteorol. Soc.* **77**: 437–471.
- Kaser G, Osmaston H. 2002. *Tropical glaciers*. Cambridge University Press: Cambridge.
- Kirshbaum DJ, Durran DR. 2004. Factors governing cellular convection in orographic precipitation. *J. Atmos. Sci.* **61**: 682–698.
- Kistler R, Kalnay E, Collins W, Saha S, White G, Woollen J, Chelliah M, Ebisuzaki W, Kanamitsu M, Kousky V, van den Dool H, Jenne R, Fiorino M. 2001. The NCEP–NCAR 50-year reanalysis: Monthly means CD-ROM and documentation. *Bull. Am. Meteorol. Soc.* **82**: 247–267.
- Klemp JB, Wilhelmson RB. 1978. The simulation of three-dimensional convective storm dynamics. *J. Atmos. Sci.* **35**: 1070–1096.
- Klute F. 1916. Beobachtungen über Zackenfirm (Büßerschnee) und dessen Entstehung am Kilimandscharo. *Z. Gletscherk.* **8**: 289–305.
- Lintner BR, Neelin JD. 2007. A prototype for convective margin shifts. *Geophys. Res. Lett.* **34**: L05812, DOI:10.1029/2006GL027305.
- Mölg T, Hardy DR. 2004. Ablation and associated energy balance of a horizontal glacier surface on Kilimanjaro. *J. Geophys. Res.* **109**: D16104, DOI: 10.1029/2003JD004338.
- Mölg T, Renold M, Vuille M, Cullen NJ, Stocker TF, Kaser G. 2006. Indian Ocean zonal mode activity in a multicentury integration of a coupled AOGCM consistent with climate proxy data. *Geophys. Res. Lett.* **33**: L18710, DOI: 10.1029/2006GL026384.
- Mölg T, Cullen NJ, Hardy DR, Kaser G, Klok L. 2008a. Mass balance of a slope glacier on Kilimanjaro and its sensitivity to climate. *Int. J. Climatol.* **28**: 881–892.
- Mölg T, Hardy DR, Cullen NJ, Kaser G. 2008b. Tropical glaciers, climate change, and society: Focus on Kilimanjaro (East Africa). Pp 168–182 in *Darkening peaks: Glacier retreat, science, and society*, Orlove BS, Wiegandt E, Luckman BH (eds). University of California Press: Berkeley, London.
- Mölg T, Cullen NJ, Kaser G. 2009a. Solar radiation, cloudiness and longwave radiation over low-latitude glaciers: Implications for mass balance modelling. *J. Glaciol.* **55**: 292–302.
- Mölg T, Cullen NJ, Hardy DR, Winkler M, Kaser G. 2009b. Quantifying climate change in the tropical mid-troposphere over East Africa from glacier shrinkage on Kilimanjaro. *J. Climate*, in press. DOI: 10.1175/2009JCLI2954.1
- Mutai CC, Ward MN. 2000. East African rainfall and the tropical circulation/convection on intraseasonal to interannual timescales. *J. Climate* **13**: 3915–3939.
- Mwangi MN, Desanker PV. 2007. Changing climate, disrupted livelihoods: The case of vulnerability of nomadic Maasai pastoralism to recurrent droughts in Kajiado district, Kenya. *Eos Trans. Am. Geophys. Union* **88**: Fall Meet. Suppl., Abstract GC12A-02.
- Nicholson SE. 2000. The nature of rainfall variability over Africa on time scales of decades to millennia. *Global and Planetary Change* **26**: 137–158.
- Nicholson SE, Yin X. 2001. Rainfall conditions in equatorial East Africa during the nineteenth century as inferred from the record of Lake Victoria. *Clim. Change* **48**: 387–398.
- Pielke RA, Cotton WR, Walko RL, Tremback CJ, Lyons WA, Grasso LD, Nicholls ME, Moran MD, Wesley DA, Lee TJ, Copeland JH. 1992. A comprehensive meteorological modeling system – RAMS. *Meteorol. Atmos. Phys.* **49**: 69–91.
- Rabus B, Eineder M, Roth A, Bamler R. 2003. The shuttle radar topography mission – A new class of digital elevation models acquired by spaceborne radar. *J. Photogramm. Remote Sensing* **57**: 241–262.
- Roe GH. 2005. Orographic precipitation. *Ann. Rev. Earth Planet. Sci.* **33**: 645–671.
- Rögnvaldsson Ó, Bao J-W, Ólafsson H. 2007. Sensitivity simulations of orographic precipitation with MM5 and comparison with observations in Iceland during the Reykjanes Experiment. *Meteorol. Z.* **16**: 87–98.
- Røhr PC, Killingtveit Å. 2003. Rainfall distribution on the slopes of Mt. Kilimanjaro. *Hydrol. Sci. J.* **48**: 65–77.
- Rotunno R, Houze RA. 2007. Lessons on orographic precipitation from the Mesoscale Alpine Programme. *Q. J. R. Meteorol. Soc.* **133**: 811–830.
- Schafer R, Avery SK, Gage KS. 2003. A Comparison of VHF wind profiler observations and the NCEP–NCAR reanalysis over the tropical Pacific. *J. Appl. Meteorol.* **42**: 873–889.
- Schär C. 2002. Mesoscale mountains and the larger-scale atmospheric dynamics: A review. Pp 29–42 in *Meteorology at the Millennium*, Pearce RP (ed.). Academic Press: New York.
- Troll C, Wien K. 1949. Der Lewisgletscher am Mount Kenya. *Geogr. Ann.* **31**: 257–274.
- Walko RL, Cotton WR, Meyers MP, Harrington JY. 1995. New RAMS cloud microphysics parameterization. Part I: The single-moment scheme. *Atmos. Res.* **38**: 29–62.
- Webster PJ, Moore AM, Loschnigg JP, Leben RR. 1999. Coupled ocean–atmosphere dynamics in the Indian Ocean during 1997–98. *Nature* **401**: 356–360.
- Xie P, Arkin PA. 1997. Global precipitation: A 17-year monthly analysis based on gauge observations, satellite estimates, and numerical model outputs. *Bull. Am. Meteorol. Soc.* **78**: 2539–2558.
- Zängl G, Gantner L, Hartjenstein G, Noppel H. 2004. Numerical errors above steep topography: A model intercomparison. *Meteorol. Z.* **13**: 69–76.